Droplet-based millifluidic synthesis of a proton-conducting sulfonate metal–organic framework

Chao Sun [a,b,e], Matthew Barton [b], Christopher M. Pask [b], Mohamed Edokali [a], Lina Yang [a],
Andrew J. Britton [a,c], Stuart Micklethwaite [a,c], Francesco Iacoviello [d], Ali Hassanpour [a],
Maximilian Besenhard [a,d], Rik Drummond-Brydson [a,c], Ke-Jun Wu [a,e,*], Sean M. Collins [a,b,c,*]

[a] *School of Chemical and Process Engineering, University of Leeds, Leeds LS2 9JT, UK*
[b] *School of Chemistry, University of Leeds, Leeds LS2 9JT, UK*
[c] *Bragg Centre for Materials Research, University of Leeds, Leeds LS2 9JT, UK*
[d] *Department of Chemical Engineering, University College London, London WC1E 7JE, UK*
[e] *Zhejiang Provincial Key Laboratory of Advanced Chemical Engineering Manufacture Technology, College of Chemical and Biological Engineering, Zhejiang University, Hangzhou, 310027, China*

ABSTRACT

Metal–organic frameworks (MOFs) have emerged as promising candidate materials for proton exchange membranes (PEMs), due to the control of proton transport enabled by functional groups and the structural order within the MOFs. In this work, we report a millifluidic approach for the synthesis of a MOF incorporating both sulfonate and amine groups, termed Cu-SAT, which exhibits a high proton conductivity. The fouling-free multiphase flow reactor synthesis was operated for more than 5 h with no reduction in yield or change in the particle size distribution, demonstrating a sustained space–time yield up to 131.7 kg m^{-3} day^{-1} with consistent particle quality. Reaction yield and particle size were controllably tuned by the adjustment of reaction parameters, such as residence/reaction time, temperature, and reagent concentration. The reaction yields from the flow reactor were 10–20% higher than those of corresponding batch syntheses, indicating improved mass and heat transfer in flow. A systematic exploration of synthetic parameters using a factorial design of experiments approach revealed the key correlations between the process parameters and yields and particle size distributions. The proton conductivity of the synthesized Cu-SAT MOF was evaluated in a mixed matrix membrane model PEM with polyvinylpyrrolidone and polyvinylidene fluoride polymers, exhibiting a promising composite conductivity of 1.34 ± 0.05 mS cm^{-1} at 353 K and 95% relative humidity (RH).

1. Introduction

Metal–organic frameworks (MOFs), a class of coordination polymers, are composed of metal ions or clusters interconnected by organic linker molecules in extended three-dimensional networks [1,2]. The wide variety of both the organic and inorganic components in these structures demonstrated to date, and particularly the range of functional groups that can be incorporated to coordinate metal sites or modify interior pore structures, endow MOF materials with versatile functions from gas storage [3,4], chemical separations [5], and catalysis [6,7] to proton conduction [8–11]. Proton exchange and ion transport membranes for fuel cells and energy conversion and storage applications benefit from the well-defined crystal structures and diverse functional group

chemistry controlled by linker selection in MOFs [12].

Sulfonate MOFs are considered to be promising materials for proton conduction, as sulfonic acid groups can provide proton hopping sites which promote proton transfer within the material [13]. Sulfonates are typically weakly coordinating moieties, favoring the formation of well-defined metal-sulfonate coordination motifs with soft metal ions (e.g. Cu^{2+}, Ag^+, Cd^{2+}, Ba^{2+}) [14]. Cu-based sulfonate MOFs incorporating N-donor ligands to form 3D frameworks have been reported [15], where N-donor ligands appear to serve a structure-directing role to promote 3D network formation in sulfonate MOFs [14,16]. Sulfonate MOFs with triazolate ligands present elevated proton conductivity, attributed to the complementary acid – base and hydrogen bonding interactions of the sulfonate and amine groups [17,18]. However, compared with other

---

MOF families (e.g. carboxylate and imidazolate MOFs), much remains unknown about the crystallization processes of sulfonate MOFs and their dependence on synthesis parameters.

The breadth of MOF research has inspired the development of different synthetic methodologies. Hydrothermal synthesis [19–21] and solvothermal synthesis [22–24] are two common methods for MOF production. Both methods, however, often require reaction times of hours or days and suffer from batch-to-batch variability due to non-uniform reagent concentrations and low heat transfer in batch reactors. Recently, synthetic procedures for MOFs utilizing ultrasound [25,26], microwave radiation [27–29], mechanochemistry [30,31] and electrochemistry [32,33] have also been reported. Compared with these emerging alternatives to batch syntheses, continuous reactors preserve the crystal growth process as in batch reactions with improved mass and heat transfer, offering scalability through reduced reaction time and parallelizable, continuously operable flow reactors with improved uniformity of the target product.

Continuous synthesis methods such as microfluidic and millifluidic technologies, in which a chemical reaction occurs in a flowing stream rather than in a fixed batch vessel [34], can offer tight control over synthetic conditions and are favored in applications ranging from nanomaterials fabrication [35–37] to drug delivery [38,39]. Continuous synthesis allows for faster reactions because high surface area to volume ratios can enhance higher heat transfer in microreactors, and reagents undergo rapid mixing when flowing through reactor tubing [40,41]. Applied to MOFs, microfluidic synthesis has been shown to enable the continuous production of MOFs in several minutes at lower temperatures than those used in traditional solvothermal syntheses, with simultaneous control of the reaction parameters to synthesize MOFs with targeted properties [42].

Reaction yields and MOF particle sizes are particularly irreproducible in scaled-up batch reactions, as the depletion of metal ions and linkers in batch processes affects the kinetics of the oligomerization reaction and the nucleation and growth rates [43,44]. Two-phase droplet flow systems, including slug flow, offer a promising route to fabricate MOF particles whilst simultaneously inhibiting channel clogging and enhancing particle size control [45]. Because each droplet is essentially a miniature batch reactor, this ensures a narrow residence time distribution, which is difficult to achieve in a single phase microreactor. In addition, vortices within the droplets further enhance the mixing and the heat and mass transfer [46]. This results in droplets which are highly uniform in terms of chemical composition and reaction temperature, providing a highly controlled environment for chemical reactions to take place. The droplets are isolated from the reaction channel walls by using a second phase as an inert 'carrier', which can eliminate reactor fouling due to the precipitation of reactants or products, providing a stable reaction environment during continuous synthesis [47]. The development of continuous syntheses for a number of carboxylate and imidazolate MOFs [48–53] now prompts the exploration of such techniques for the distinct coordination chemistry of sulfonate MOFs.

Despite promising proton conductivity characteristics, the brittleness and poor mechanical strength of MOFs [54,55] often precludes their direct use in membranes for PEM fuel cell applications. Nafion polymer membranes are the most commonly used membranes in fuel cells because of their good proton conductivity [56]. However, Nafion manufacturing depends on toxic precursors and highly reactive intermediates, presenting hazards as well as contributing to high production costs [57,58]. As an alternative to Nafion, mixed-matrix membranes (MMMs) are fabricated by mixing inorganic/inorganic–organic materials and a polymer matrix and are also promising for PEM applications [59]. A key strategy for MMMs is to improve the properties of polymers with intrinsically poor proton conductivity. One such polymer system is the polyvinylpyrrolidone (PVP)/polyvinylidene fluoride (PVDF) polymer blend. PVDF exhibits excellent mechanical strength and good stability [60,61], whilst PVP imparts hydrophilic

properties to compensate for the native hydrophobicity of PVDF for PEM applications [62]. However, the PVP/PVDF blends do not exhibit substantial proton conductivity.

Here we evaluate a sulfonate MOF prepared by millifluidic synthesis incorporated into a PVP/PVDF MMM as a candidate composite membrane for fuel cell applications. We focus on Cu-SAT, a MOF consisting of Cu^{2+} centers coordinated with sulfonate and triazolate groups, a known candidate material for proton conducting MMMs [15]. In order to fabricate this MOF with consistent properties, a self-designed droplet-based microreactor delivering a stable slug flow pattern was employed to continuously synthesize Cu-SAT with controlled reaction yields and sample particle size. We have carried out single crystal and powder X-ray diffraction as well as electron diffraction and spectroscopic analyses to confirm the structure and composition of Cu-SAT. Using a factorial design of experiments (DoE) approach, we reveal the trade-offs between continuous synthesis process parameters (residence time, temperature and reagent concentrations) and the reaction yield, MOF particle size, and the particle size distribution. Finally, we report the proton conductivities of Cu-SAT MOF-based membranes fabricated by incorporating the synthesized material within PVP and PVDF polymers to highlight the PEM performance properties.

2. Experimental

2.1. Materials

1,5-Naphthalenedisulfonic acid tetrahydrate (H$_2$NDS, Molecular Weight: 360.36 g/mol), 1,2,4-triazol-4-amine (T4A, Molecular Weight: 84.08 g/mol), copper nitrate hemi(pentahydrate) (Molecular Weight:232.59 g/mol), N, N-dimethylformamide (DMF, $\geq$ 99.9%), 2-propanol (IPA, $\geq$ 99.9%), silicone oil (viscosity: 150 CST, density: 1.075 g/mL, employed as the continuous phase in continuous synthesis), polyvinylpyrrolidone (PVP) [M$_W$ 360,000], and polyvinylidene fluoride (PVDF) [M$_W$ 534,000] were purchased from Sigma Aldrich and used as received.

2.2. Batch synthesis of the Cu-SAT MOF

The batch reaction was adapted from the procedure reported by Moi *et al.* [15]. First, 8.4 mg (0.1 mmol) T4A was dissolved in deionized water in a 20 mL glass vial, then 23.2 mg (0.1 mmol) of copper nitrate and 36 mg (0.1 mmol) of H$_2$NDS were dissolved in this solution successively. Next, DMF was added to the initial aqueous solution of the precursors. The volume ratio of the DMF-water solvent was 10:3, and the total volume of solvent for the reaction was fixed between 2.6 and 3.9 mL. The prepared chemical solutions were heated by immersing reaction vials in an oil bath at temperatures ranging from 80 to 110 °C for reaction times between 60 and 300 min. At the end of the set reaction time, blue solids were recovered by vacuum filtration and washed with 5 mL DMF three times. Samples were then dried in an oven at 80 °C for 10 h. For the scaled-up batch reaction, the reagents and solvents were scaled up by a factor of 3.3. Reaction procedures were otherwise the same as for the small-scale batch reactions. To examine the effect of stirring on batch reactions, a stir bar with a length of 10 mm was placed in the reaction vial with a stirring speed of 500 revolutions/min during the reaction, and identical reaction procedures were followed as for the unstirred batch reaction. Based on the identified crystal structure (single crystal XRD, this work), the molecular weight of Cu-SAT is 688.64 g mol^{-1}. The synthetic yields were calculated using recovered sample weight (the weight of the dried sample on the filter paper minus the weight of the filter paper) divided by the weight expected for complete conversion of the precursors to Cu-SAT.

2.3. Continuous synthesis of Cu-SAT MOF

As T4A and H$_2$NDS ligands undergo a side reaction with copper

nitrate at room temperature, in order to achieve better mixing of precursors and form stable droplets for continuous synthesis of Cu-SAT MOF, the two ligands (combined) and the Cu^{2+} nitrate precursor were introduced via two different syringes. In the droplet-based millifluidic setup, glass syringes (25 mL, SGE) were used to carry chemical precursors and silicone oil, a cross connector (P-723, IDEX) was used to mix all precursors simultaneously and form stable slugs within the continuous silicone oil phase, with each slug containing the same volume and concentration of reagents. For stable slug flow, we found a 1:1 ratio to be optimal, with variations producing shorter and longer slugs that were, however, unstable. Before carrying out a reaction, the silicone oil and the reagent solutions were degassed in a sonicator at 60 °C for 1 h. All reagents used for continuous synthesis were prepared with a ratio of DMF to water equal to 10:3. A preheating step was used to ensure all solutions reached a well-defined temperature prior to mixing and droplet segmentation. The preheating system consisted of three PFA inlet tubings (1/32 in. ID, Adtech) with a 50 cm length immersed in the oil bath ahead of the cross connector. The reactor tubing (PFA, 1/16 in. ID, 10 m, Adtech) was coiled around a circular metal mesh cylinder (diameter ~ 10 cm) and the reaction started after the oil bath reached the set temperature.

The flow rates of the reagent solutions and the silicone oil were set to be equal. The residence time was taken as the volume of the reactor divided by total flow rate, a suitable estimate for segmented flow. Flow rates and oil bath temperatures were controlled to give residence times and reaction temperatures from 60 to 120 min and from 80 to 90 °C, respectively. After the reaction, synthesized particles together with unreacted reagents and silicone oil were collected in a vial and separated via centrifugation at 6800 rpm for 10 min. The solvent was then decanted to recover reusable silicone oil, and the product (a blue powder) was washed with 10 mL IPA three times and recovered by vacuum filtration. The recovered solid powder was then dried in an oven at 80 °C for 10 h.

2.4. Computational fluid dynamics (CFD) simulation methods

Simulations were performed using ANSYS Fluent software (ANSYS 2022R2). In this work, incompressible two–phase (silicone oil–DMF/water mixture) flow is considered, where the silicone oil and the DMF/water mixed solvent are the continuous and dispersed phases, respectively. The interface is tracked by the volume of fluid method, which solves a single set of conservation equations for both phases. This set of equations comprises an equation of continuity:

$$\nabla \bullet (\rho \mathbf{u}) = 0 \tag{1}$$

and an equation of motion:

$$\frac{\partial(\rho \mathbf{u})}{\partial t} + \nabla \bullet (\rho \mathbf{u}\mathbf{u}) = -\nabla P + \nabla \bullet \left[\mu \left(\nabla \mathbf{u} + \nabla \mathbf{u}^T \right) \right] + \rho g + F_s \tag{2}$$

where ρ is the volume-averaged density, $\mathbf{u}$ is the velocity vector, t is time, P is the pressure, μ is the dynamic viscosity, g is the gravitational acceleration, and F_s is the continuum surface tension.

The volume-averaged properties are defined as:

$$\rho = \alpha_o \rho_o + (1 - \alpha_w)\rho_w \tag{3}$$

where α_o and ρ_o represent the volume fraction and density of the silicone oil, α_w and ρ_w are the volume fraction and density of the DMF/water mixture. The dynamic viscosity is further defined as:

$$\mu = \alpha_o \mu_o + (1 - \alpha_w)\mu_w \tag{4}$$

where subscripts likewise refer to the silicone oil (o) and DMF/water mixture (w), respectively. The volume fraction of each liquid phase is calculated by solving the equation:

$$\frac{\partial \alpha_i}{\partial t} + \mathbf{u} \bullet \nabla \alpha_i = 0 \tag{5}$$

The geometric model used in the simulation is shown in Fig. S1. The system has one inlet (the horizontal one) for the continuous phase and two inlets (the vertical ones) for the dispersed phases. The velocity-flow inlet boundary condition was used at all three inlets. The outlet was defined as a pressure outlet, and the no-slip boundary condition was used at the walls. The values of the density and viscosity of the two phases and the interfacial tension are listed in Table S1. The analysis to evaluate the sensitivity of mesh size on the droplet length was conducted as shown in Table S2. After the grid independence test, a mesh consisting of 87,172 cells was adopted to ensure a reasonable trade-off between simulation accuracy and computational cost. The numerical simulation was verified by comparing the simulated droplet length ($V_{inlet-1} = 0.002$ m s^{-1}, $V_{inlet-2} = V_{inlet-3} = 0.001$ m s^{-1}) with photographs of the experimental system (Fig. 2). The relative difference in the length of the droplets observed in the experimental system and the simulations was <5%.

2.5. Linear response surface modelling of continuous synthesis

A minimal factorial DoE approach was carried out using the millifluidic reactor for three reaction parameters: temperature, time, and reagent concentration. The response variables were selected as yield, particle size, and particle size interquartile range (IQR). In total, a two-level, three factor design was set up to give 11 experiments (two levels for each reaction parameter with three repeats at the center of the resulting parameter cube, see also Fig. S2). Linear response modelling was performed using Minitab (version 21.2). An analysis of variance was carried out to identify statistically significant terms for linear response model fitting. Terms associated with low probability values (p-values) were excluded from model fitting. The p-values together with an inspection of the distribution of contributions of all terms were used to select retained terms, targeting the minimum number of terms to describe the response. For yield and mean particle size, a clear separation between significant terms and terms with low p-values (<0.05) was observed. For particle size IQR, all terms showed effects and were retained in the model fitting.

2.6. Membrane fabrication

The MMMs were fabricated using 60% by weight (wt%) of Cu-SAT incorporated into PVP and PVDF (denoted as MMM-60 wt%). Typically, 180 mg of continuously synthesized Cu-SAT were ground in a mortar and pestle and dispersed in 1.8 mL DMF by sonication for 20 min. Then, 30 mg PVDF and 90 mg PVP were added successively and dissolved in the Cu-SAT suspension in DMF while stirring at room temperature for 300 min to obtain a homogeneous gel. This gel was poured onto a high-temperature resistant glass and cast using a BGO 209/2 adjustable applicator (Biuged Laboratory Instruments Co., Ltd). The thickness of membrane was adjusted by changing the gap between the glass and the casting blade; in this study the gap value in the adjustable applicator was set to 100 μm. The membrane was then dried at 70 °C for 1 h in a vacuum oven to remove excess DMF. The solidified membrane was finally washed with deionized water three times and then dried at room temperature.

2.7. Materials characterization

Powder X-ray diffraction patterns were recorded using a Bruker D2 diffractometer (Cu Kα λ = 1.54 Å, 2θ scan range = 5° − 50°). Single crystal X-ray diffraction measurements were carried out at 100 K on a Rigaku SuperNova diffractometer equipped with an Atlas CCD detector and connected to an Oxford Cryostream low temperature device using mirror monochromated Cu Kα radiation (λ = 1.54184 Å) from a

microfocus X-ray source. The structure was solved by intrinsic phasing using SHELXT [63] and refined by a full matrix least squares technique based on F^2 using SHELXL2014 [64]. Vesta software (version 3.5.7) was employed to produce calculated XRD patterns of Cu-SAT from the single crystal structure.

The morphologies of the MOF samples were characterized by light microscopy (LM, Olympus, BX51) and scanning electron microscopy (SEM, Hitachi/TM-3030Plus, equipped with a backscattered electron detector and operated at 15 kV accelerating voltage). Particle sizes were measured from light micrographs using ImageJ, determined as the average of (a) the length taken as the longest dimension of the particle and (b) the width perpendicular to the length. More than 100 particles were measured for each sample. Cryo-SEM was carried out using an FEI Helios G4 CX cryo-FIBSEM, operated at 10 kV and equipped with a Quorum Technologies PP3010 cryo-stage and an Oxford instruments 150 X-Max energy dispersive X-ray spectroscopy (EDS) detector, to check the thickness, surface morphology, and elemental composition of the hydrated membrane.

FTIR spectra of the MOF samples and membranes were obtained using a Bruker Vertex 80 V Fourier Transform Infrared (FTIR) spectrometer with a diamond prism Attenuated Total Reflection (ATR) crystal. Using a 6 mm aperture, data were collected for wavenumbers between 500 and 4000 cm^{-1} and averaged over 16 scans. Cu-SAT crystals were ground to a fine powder before FTIR measurements. Thermogravimetric analyses (TGA) were carried out using a Netzsch STA 449F3 instrument with a heating rate of 10 °C min^{-1} in a nitrogen atmosphere (40 mL min^{-1}). N_2 adsorption–desorption measurements were attempted but showed generally low adsorption and did not offer physically interpretable isotherms. We infer Cu-SAT has very low if any accessible porosity for N_2.

A Thermo Scientific Flash EA2000 elemental analyser was used to detect carbon, hydrogen, nitrogen and sulphur (CHNS) in Cu-SAT samples. Briefly, this analysis entailed dropping samples into a furnace at 900 °C in a continual flow of helium. Pure oxygen was added for a few seconds to facilitate combustion. The combustion products pass through an oxidation/reduction reactor to convert them to CO_2, H_2O, N_2 and SO_2 which are then separated by gas chromatography and detected using thermal conductivity. X-ray photoelectron spectroscopy (XPS) was used to characterize the surface chemistry of the materials. The sample powder was pressed lightly onto carbon tape and adhered to a standard omicron plate. Excess powder was knocked off to obtain a uniform flat sample. The experiment was carried out in UHV ($<1 \times 10^{-9}$ mbar) on a Specs FlexMod system. The illuminating X-ray source was a monochromatic Al Kα (hν = 1486.7 eV) anode at a power of 100 W and 15 kV. A Specs Phoibos 150 hemispherical analyzer with 1D delay line detectors was used to detect the photoelectrons. The powder is insulating so to reduce any differential charging at the surface which could distort the spectra, an electron flood gun (energy 1 keV and current 75 μA) was used to charge neutralize the sample. Survey spectra were obtained with a pass energy of 50 eV, a step width of 1 eV and a dwell time of 0.1 s. High resolution spectra were collected with a pass energy of 30 eV, a step width of 0.1 eV and a dwell time of 0.1 s. After collecting the spectra, the data was analyzed using CasaXPS software. Binding energies were calibrated using the C-C C1s peak at 285 eV and the intensity was calibrated using a previously calculated transmission function for the specific instrument settings. All spectra were fitted with a Shirley background and the peak areas were determined. We quantified the relative atomic percentages using these peak areas and the respective relative sensitivity functions for each peak.

Analytical scanning transmission electron microscopy (STEM) was employed to analyze individual microscopic crystals using scanning electron diffraction (SED). Data was acquired using a JEOL ARM300CF transmission electron microscope at the Diamond Light Source, fitted with a high-resolution pole piece, cold field emitter, and JEOL spherical aberration correctors in both the probe forming and image forming optics. The instrument was operated at 300 kV with a gun lens setting

calibrated to give a probe current of 1.9 pA. The diffraction-limited probe diameter was taken as $1.22\lambda/\alpha$ where λ is the electron wavelength at 300 kV (1.97 Å) and the convergence angle α is 0.8 milliradians, defined by a 10 μm condenser aperture. A Merlin-medipix direct electron detector was used to record the electron diffraction pattern at each probe position (step size ca. 5.2 nm) with an exposure time of 1 ms per probe position. Assuming a circular probe with a diffraction-limited diameter (3 nm), the total fluence was approximately 17 electrons $Å^{-2}$. SED data was acquired over a raster scan comprising 256 × 256 probe positions and each diffraction pattern comprised 512 × 512 pixels. Following SED acquisition, EDS maps were acquired from the same regions using a larger probe current (obtained with a 100 μm condenser aperture) to generate sufficient X-ray counts. SED data were processed using pyXem, an open source Python library [65]. Images and diffraction patterns were calibrated using a standard gold cross-grating with a period of 500 nm. Relative rotation of the diffraction pattern and the raster image was calibrated using a MoO_3 standard.

The three-dimensional microstructure of a representative Cu-SAT and PVP/PVDF membrane was investigated using X-ray micro-computed tomography (Zeiss Xradia 620 Versa operated at 50 kV and 90 mA). 1,101 radiographs were acquired over a 360° sample rotation range with an exposure time of 10 s per radiograph. The sample was mounted on a steel pin and placed between the X-ray source and a 2 k × 2 k detector providing a voxel resolution of 364 nm using a 40 × objective magnification. Raw transmission images were reconstructed using a commercial image reconstruction software package (Zeiss XMReconstructor, Carl Zeiss X-ray Microscopy Inc., Pleasanton, CA), which employs a filtered back-projection algorithm. The 3D reconstructed volume of the sample was analyzed with the Zeiss proprietary software, TXM3DViewer.

2.8. Proton conductivity

An important parameter to evaluate PEM performance is the proton conductivity (σ, S cm^{-1}) defined as:

$$\sigma = \frac{L}{AR} \tag{6}$$

where L is the length between the two electrodes (cm), A is the membrane area (cm^{-2}, equal to the width × thickness of the hydrated membrane, as measured by Cryo-SEM), and R is the resistance of membrane (Ω). R is often measured by electrochemical impedance spectroscopy (EIS) and the intercept at the axis corresponding to the real part of the complex impedance (Z′) is taken as the resistance [56] or by Cyclic Voltammetry (CV) using the slope of the voltage versus current response. A BT-110 conductivity clamp (L = 0.425 nm) was used to measure the in-plane resistance and hence ionic conductivity of fabricated membrane samples using a Gamry 1010E electrochemical workstation. A four electrode setup was used for the CV test with a scan rate of 10 mV/s between −0.1 V and 0.1 V. EIS was measured between frequencies of 1 Hz and 1 MHz using a two electrode setup in order to minimize artifacts, such as additional inductive and capacitive features arising from the testing coaxial cables [66].

All EIS and CV measurements were performed 30 min after the testing temperature reached the set value. Before resistance testing, the membrane was placed in a 95% relative humidity (RH) chamber (Memmert HCP150) at room temperature for 12 h to fully hydrate the membrane, matching commonly applied RH equilibration conditions prior to testing [67,68]. Fig. S17a and b present the EIS and CV results of MMM-60 wt% measured at different times when the temperature reached 70 °C in 95% RH, indicating the highest proton conductivity was reproducibly achieved 30 min after the testing temperature reached the set value. The subsequent reduction in the observed proton conductivity was attributed to the finite stability of Cu-SAT at elevated temperatures (see also Results and Discussion) or gradual dehydration of
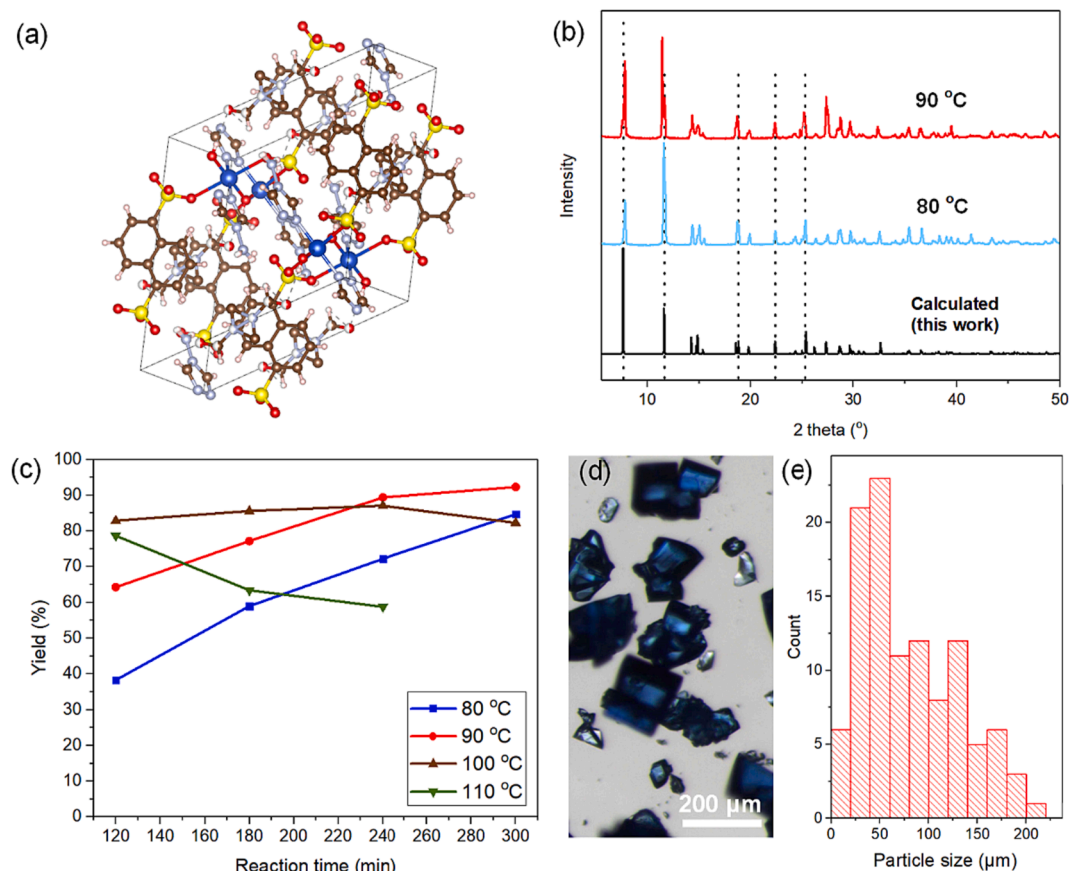
Fig. 1. Single-crystal structure of Cu-SAT and results of batch synthesis under different reaction parameters: (a) Depiction of the crystal structure of Cu-SAT MOF (S, yellow; Cu, blue; O, red; N, lavender; H, pink; C, gray), (b) XRD patterns of batch samples synthesized under different temperatures with 120 min reaction time compared with single crystal simulated pattern, (c) percentage yield of Cu-SAT achieved for different synthesis times and temperatures, (d) light micrograph of Cu-SAT synthesized at 80 °C for 120 min and (e) associated histogram of the particle size distribution. (For interpretation of the references to color in this figure legend, the reader is referred to the web version of this article.)

the polymer matrix at elevated temperatures; signs of dehydration were visible on removal of membranes from the testing chamber. We therefore report the membrane conductivity at this reproducible 30 min point in order to determine the achievable conductivity, RH, and temperature response, without further optimization of the polymer composition or Cu-SAT stability.

The activation energy (E_a) for membrane proton conduction was determined via the Arrhenius relationship [69]:

$$\ln(T\sigma) = \ln(\sigma_0) - \left(\frac{E_a}{R}\right)\left(\frac{1000}{T}\right) \tag{7}$$

where T is testing temperature (K), σ is the proton conductivity (S cm^{-1}), σ_0 is the pre-exponential factor (S (K cm)$^{-1}$) and R is the ideal gas constant (8.314 J (mol K)$^{-1}$). E_a was determined from the slope of this Arrhenius plot.

3. Results and discussion

3.1. Batch synthesis of Cu-SAT MOF

Cu-SAT synthesis has been previously reported by Moi *et al.* using a 180-min batch synthesis at 80 °C [15]. In order to resolve a discrepancy between the experimental powder XRD and the reported Cu-SAT crystal structure [15], we carried out a single crystal XRD (SC-XRD) structure determination for our own replicate batch synthesis at 80 °C (Fig. 1a). We found that Cu-SAT can be described by a monoclinic unit cell (*C 2/m*) with lattice parameters $a = 15.2535(7)$ Å, $b = 6.7877(2)$ Å, $c = 14.1582(6)$ Å and $\beta = 125.469(7)°$ (denoted 'this work', deposited at the

CCDC, reference number 2247539). The crystallographic parameters of Cu-SAT are listed in Table S3 in the Supporting Information (SI). This structure is similar to the previously reported structure for Cu-SAT (CCDC reference number 1995454) in terms of the coordination and molecular packing with Cu^{2+} octahedrally coordinated by *trans*-coordinated pairs of hydroxyl, T4A, and NDS ligands. The Cu^{2+} centers form quasi-1D chains which are linked along the chain by two of the sulfonate oxygens and two of the T4A N-donor sites at the base of the triazolate ring. The NDS ligands bridge between the Cu^{2+} chains, positioned with aromatic ring faces aligned and interleaved by residual DMF molecules. The third un-coordinated oxygen on each of the sulfonate SO$_3$ groups and the R-NH$_2$ groups of T4A align parallel with the Cu^{2+} chains (*b*-axis). As shown in Fig. 1b, XRD patterns of Cu-SAT made in batch at different temperatures match all peak positions observed in the single crystal simulated result, and samples prepared at 80 °C with different reaction times also presented consistent XRD patterns (Fig. S3).

We have further varied reaction time, reaction temperature, and concentration of reagents to map their effects on the reaction yield and particle size and to establish suitable parameters for continuous synthesis. Fig. 1c presents yields for Cu-SAT solvothermal batch syntheses at reaction temperatures ranging between 80 and 110 °C and for reaction times ranging between 120 and 300 min. Gravimetric yields were justified to track reaction yield, given the apparent phase-purity of the XRD patterns and the recovery of consistent faceted blue particles as observed by light microscopy (Fig. 1b and d). For 80 °C, the yield continued to increase up to 300 min, with a plateau in the yield observed after 240 min at 90 °C, indicating faster reaction kinetics with increased temperature. Maximum yields of approximately 90% were recorded at
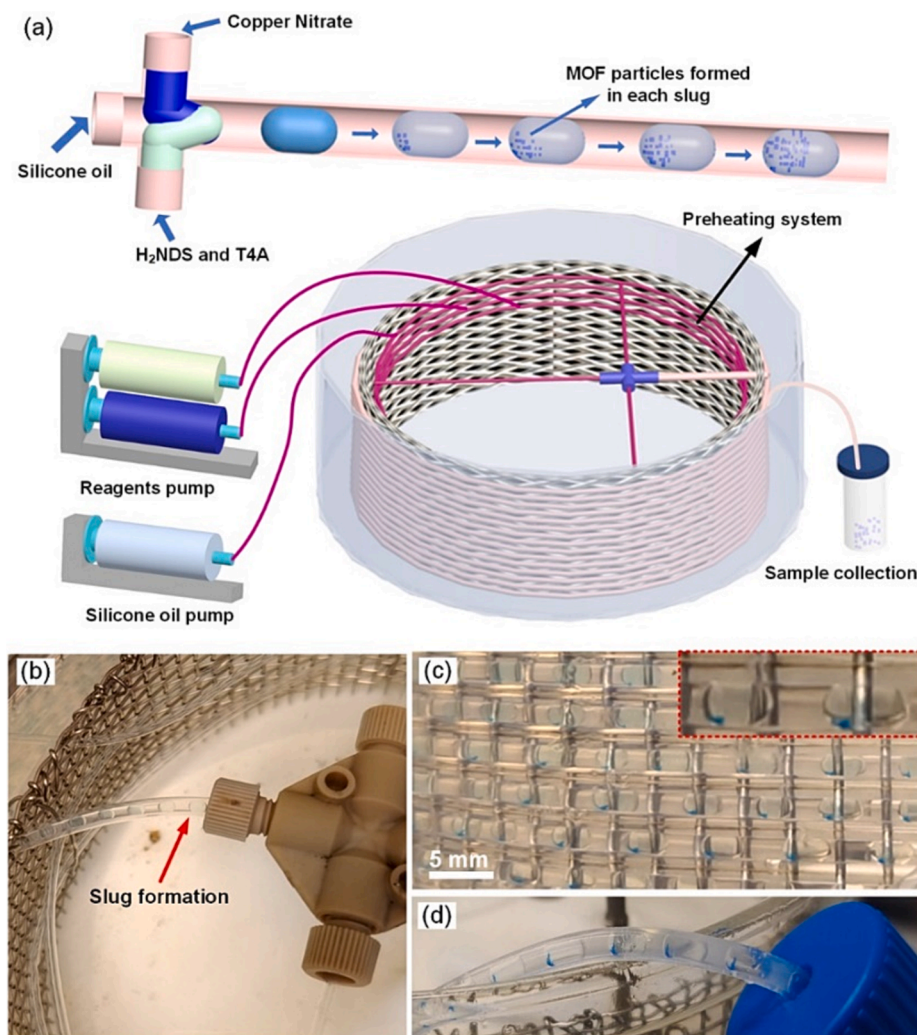
Fig. 2. Transferring batch synthesis of Cu-SAT to continuous synthesis: (a) schematic diagram of the setup for two phase continuous synthesis of Cu-SAT MOFs, digital pictures of (b) slug formation at the inlet, (c) particle formation in the flow reactor and (d) sample collection at the reactor outlet.

90 °C. Above 90 °C, however, yields decreased. At 110 °C, a change in the solvent color from transparent blue to opaque black indicated decomposition of reagents over the course of reactions at elevated temperatures. The effect of solution concentration on yield was also studied by adjusting the total volume of the reaction mixture (2.6, 3.25 and 3.9 mL of solvents, fixed precursor quantities, SI Table S4), and exhibited a consistent decrease in yield for reduced reagent concentrations.

Fig. 1d and e presents a light micrograph and an associated histogram of the particle size distribution of Cu-SAT prepared at 80 °C and for a 120 min reaction time. The particles exhibit a characteristic blue color and possess a blocky morphology with a wide and skewed size distribution up to ~ 200 μm. Figs. S4 and S5 in the SI present additional light micrographs and box plots of particle size from different batch samples. For small-scale batch syntheses at 80 °C, an increase in reaction time from 180 min to 300 min resulted in an increase in the median particle size from 74 μm to 156 μm as well as an increase in the particle size interquartile range (IQR, a direct measure of the width of skew and non-skew distributions) from 62 μm to 83 μm. At 90 °C, both the median particle size and particle size dispersity (as recorded in the IQR) increased with longer reaction times as well. These results indicate batch synthesis is consistent with a crystal growth process comprising heterogeneous nucleation and growth as well as additional homogeneous nucleation events occurring over the course of the batch reaction. In batch reactions scaled up by a factor of 3.3 (8.6 mL of reagents rather

than 2.6 mL), the yield decreased and the sample particle size and particle size IQR increased relative to small-scale reactions, which we attribute to the poor heat and mass transfer in these batch reactions.

3.2. Continuous synthesis of Cu-SAT MOFs

In order to establish a reproducible method for Cu-SAT synthesis with higher space–time yield and particle size control, we developed a continuous synthesis for Cu-SAT using a millifluidic flow reactor. A schematic diagram of the two-phase continuous synthesis setup with a preheating system is shown in Fig. 2a. Slug flow was achieved in one step by mixing the preheated reagents (dispersed phase) with silicone oil (continuous phase) using a cross connector. This setup allowed for the simultaneous mixing and segmentation of the reagents and the formation of stable slugs (Fig. 2b). Fig. 2c shows reagent slugs all with a consistent size and with slug diameters approximately equal to the diameter of the reaction tubing, and the slug length is approximately twice the diameter of the reaction tubing; these features reflect the stable slug pattern achieved in this reactor.

CFD simulations were used to understand formation mechanism of slugs in the cross connector (Fig. 3). In the double T-junction microtube (cross connector), as the dispersed phase continuously flowed into the main channel, the front of the two dispersed phases began to meet in the main channel, ultimately resulting in the head of the dispersed phase blocking the main channel. At 7 s, the dispersed phase had completely
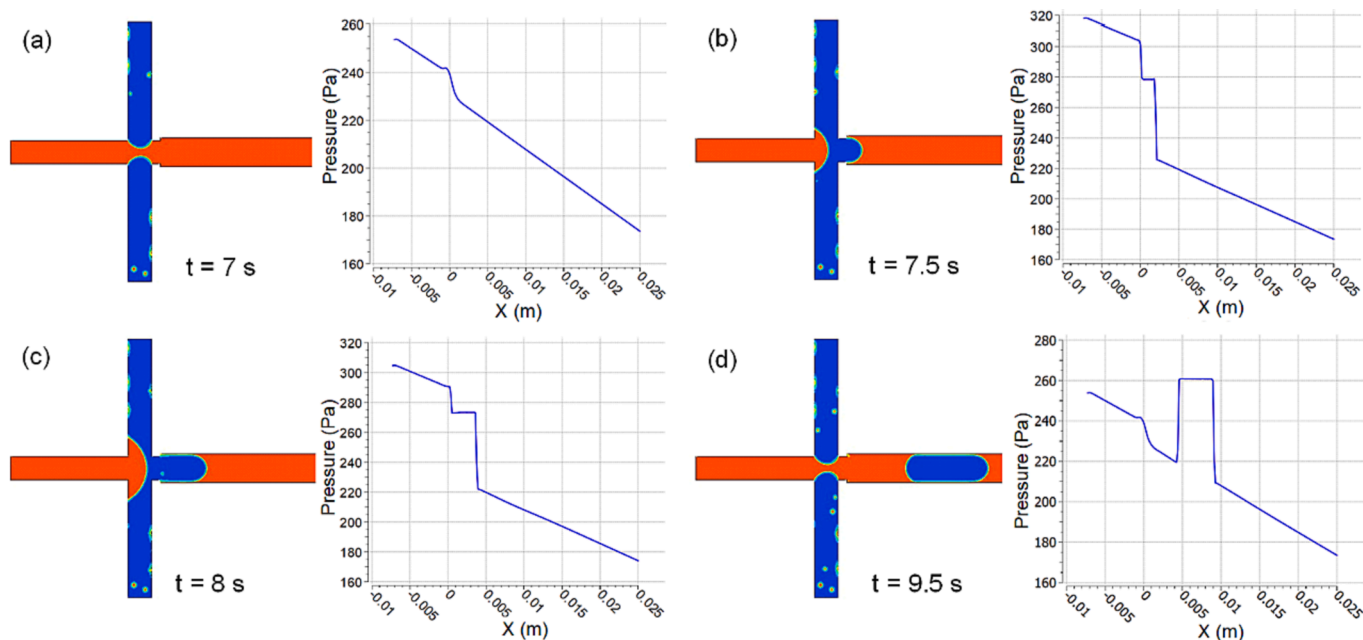
Fig. 3. The simulations of the droplet generation and pressure plots on the XZ plane when generating a droplet: Generation of droplet at (a) 7 s, (b) 7.5 s, (c) 8 s, and (d) 9.5 s.

blocked the main channel (Fig. 3a). Due to the viscous force and interfacial tension, the pressure in the main channel reached its maximum, indicating that the slug was growing, and its volume was increasing while continuing to move downstream (Fig. 3b and c). Finally, at 9.5 s, the neck of the slug detached from the dispersed phase (Fig. 3d). This process of slug generation is continuously repeated, and the slug size varies depending on the flow rate and flow rate ratio of the two phases.

At experimentally applied flow rates, the variation in slug size remained small. At flow rates giving a 120 min residence time, the slug length was approximately 3 mm or 5–10% longer than slugs at flow rates giving a 60 min residence time (Fig. S6a and b). Furthermore, changes in flow rates with different reactor lengths (7 m or 10 m), produced similar samples (Fig. 6c and d). Here, we used a 10 m reactor for stable, reproducible results within the range of flow rates used for Cu-SAT synthesis.

In experimental operation, blue crystals began to appear in each slug after one third of the residence time (40 min at 80 °C, and 20 min at 90 °C), with particles growing larger with increased reaction time. The slug pattern remained stable even as the product particles formed in the slugs and remained stable on leaving the reactor and moving to the collection vessel (Fig. 2d). Supplementary Video 1 presents a recording of the reaction process in the flow reactor.

XRD patterns from Cu-SAT samples made in flow with a residence time of 120 min under different reaction temperatures match with powder XRD patterns calculated from our single crystal structure (this work) and with samples made at 80 °C for different residence times (Fig. 4a and Fig. S7a), confirming the successful continuous synthesis of Cu-SAT. Fig. 4b presents a light micrograph of a continuously synthesized Cu-SAT sample made with 120 min residence time at 80 °C. As for batch reactions, continuously synthesized Cu-SAT appeared as uniformly blue crystals. Fig. 4c presents the particle size distribution of this sample, with sizes ranging between 20 and 120 μm, which is half of the full range of the corresponding batch samples synthesized with the same reaction temperature and matched reaction time (Fig. 1e). A continuous synthesis of Cu-SAT with 120 min residence time at 80 °C was operated for more than 5 h (equipped with syringe pumps with three syringes at a total flow rate of 0.16 mL/min, 0.08 mL/min for silicone oil and 0.04 mL/min for each of the aqueous phases using 24 mL silicone oil and 12 mL each of the aqueous phases from three 25 mL syringes) with no

reduction in yield or change in particle size, as well as no evidence of reactor fouling (Fig. 4d), demonstrating a sustained production rate of 59 mg h^{-1} with 78.6 kg m^{-3} day^{-1} space–time yield and consistent particle quality. The uniformity of particles collected for different reaction times is highlighted in the inset light micrographs.

The reaction yields of the batch and continuous reactions for different conditions are summarized in Table 1. The yields in continuous syntheses were typically 10–20% higher than those of the corresponding batch reactions under the same reaction parameters, indicating that the improved mass and heat transfer increase the rate of Cu-SAT formation in millifluidic synthesis. Batch synthesis with stirring was used to increase the heat and mass transfer in the batch process artificially. Using this method, an identical Cu-SAT crystal structure was observed (Fig. S7b), with higher yields for the stirred batch reactions than was achieved in both unstirred batch and continuous syntheses. The stirring in batch synthesis further verified that the yield increases with better heat and mass transfer during the reaction, but without any particle size control in the case of stirred batch reactions. Extended unstirred reactions (Fig. 1) and these stirred reactions (Table 1) suggested an upper limit of approximately 90% yield for Cu-SAT synthesis. The continuous synthesis approached this limit in the continuous reactor (greater than 80% yield at 90 °C and 120 min residence time). Further enhancing mass transfer by refinements in the reactor design may offer improvements at shorter residence times and lower temperatures.

As shown in Table 1, the production rate and space–time yield of continuous syntheses are much higher than those of batch reactions. We interpret these results as evidence that the chemical composition and reaction temperature are much more consistent in droplet based continuous synthesis, which provides a highly controlled environment for crystal nucleation and growth rates. The production rate and space–time yield of this reactor can reach up to 99 mg h^{-1} and 131.7 kg m^{-3} day^{-1} at 90 °C with 60 min residence time, respectively. Although a much higher production rate and space–time yield of the continuous synthesis of HKUST-1 MOF has been reported [70], our approach is an initial development of a continuous synthesis for sulfonate MOFs through the use of a small scale of reactor which is easy to control for the preliminary exploration of continuous synthesis parameters.

The stability of Cu-SAT prepared in the millifluidic reactor in aqueous solutions was tested by soaking this sample in deionized water
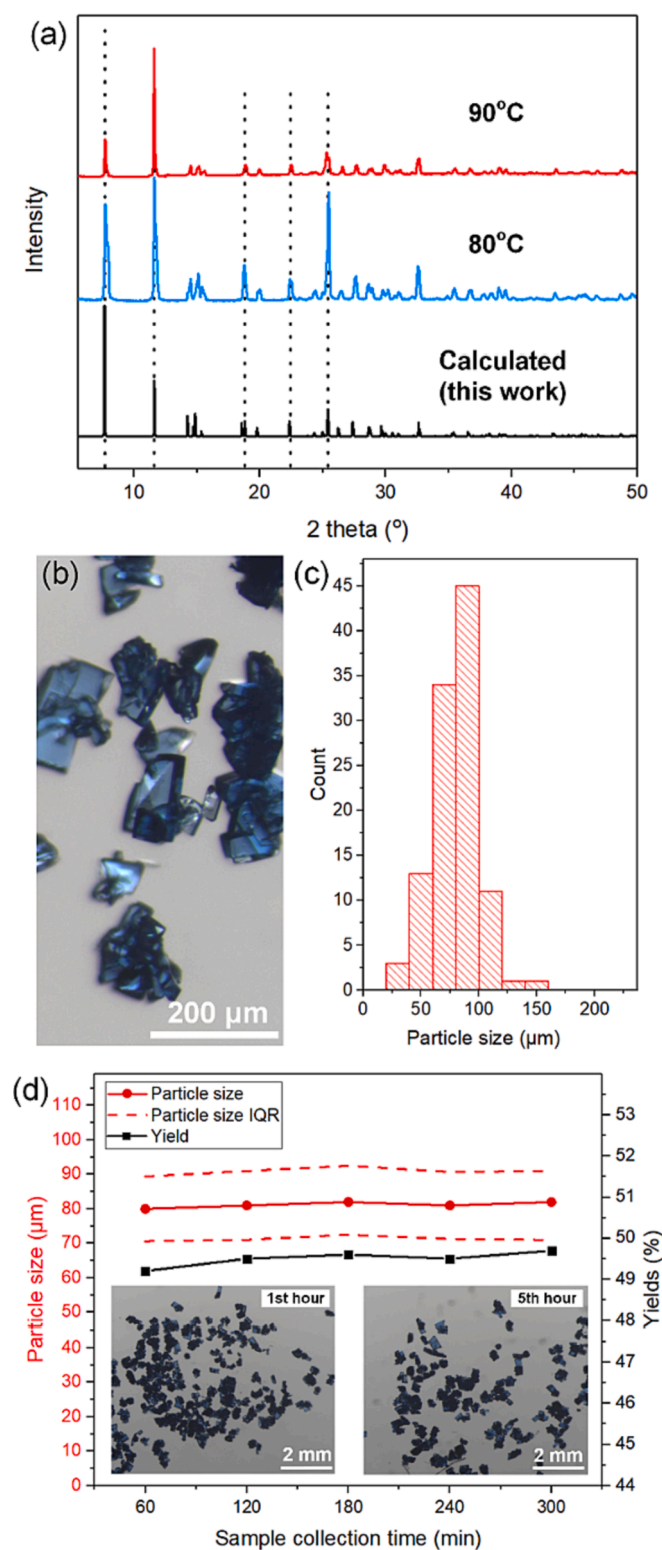
Fig. 4. Results from of samples synthesized in the millifluidic system: (a) XRD patterns of samples made at different temperatures in the millifluidic system compared with the single crystal simulated result, (b) light micrograph of Cu-SAT made in flow with 120 min residence time at 80 °C and (c) associated histogram of the particle size distribution, and (d) reaction yield and average particle size results for different operational times in one synthesis with 120 min residence time at 80 °C, inset: light micrographs of Cu-SAT MOFs collected at the first hour (left) and the fifth hours (right).

for 3 days at 25 °C and for 10 h at 80 °C, as well as in aqueous HCl (pH 2.5) for 10 h at 25 °C. XRD patterns obtained after each treatment presented similar profiles to the as-synthesized material (Fig. S7c), with new peaks emerging at low pH or high temperature after extended exposure. These peaks, likely arising from degradation phases, match those reported under similar conditions for batch-synthesized Cu-SAT [15]. ATR-FTIR spectra of samples made by both batch and continuous syntheses present similar peaks and intensities (Fig. S7d). There are strong absorption peaks at 1190, 1068, 620 and 530 cm^{-1}, which can be assigned to the main characteristic peaks of the sulfonate group [71]. The band around 1190 cm^{-1} is also attributed to the stretching vibration of the C-N bond [72]. The peak around 3300 cm^{-1} indicates amino groups in these samples [73]. Multiple absorption peaks in the range 1450 to 1650 cm^{-1} can be attributed to the skeleton vibration of the benzene rings [74], and absorption peaks in the range 650 to 900 cm^{-1} are assigned to the out-of-plane C-H bending vibration of the aromatic ring [75] in these materials. TGA for Cu-SAT prepared in the millifluidic reactor indicated no mass loss below 200 °C (Fig. S7e) followed by a series of mass losses, likely attributed to the initial release of DMF molecules between 218 and 254 °C followed by ligand decomposition.

To examine the elemental composition and chemical states in continuously synthesized Cu-SAT, CHNS and XPS analysis were carried out. Tables S5-S6 present CHNS analysis results of batch and millifluidic synthesis products, confirming agreement with the molecular formula of Cu-SAT from SC-XRD ($C_{14}H_{16}N_8O_8S_2Cu_2$ including an additional retained DMF, C_3H_7NO, per formula unit). The ratio of N to S was 3.97 ± 0.18 compared to a ratio of 4 expected for Cu-SAT without any residual DMF. As shown in Fig. S8a, the high resolution XPS spectra of this sample shows the presence of the elements Cu, O, N, C and S. The XPS analysis gave an elemental composition of 3% copper, 21.4% oxygen, 17.2% nitrogen, 54.5% carbon and 3.9% sulfur with a relative 5% uncertainty. These results match with the molecular formula of Cu-SAT. High resolution XPS spectra indicates the presence of Cu^{2+} in the Cu 2p spectra, SO_3^{2-} in the S 2p spectra and C-N bonds in the N 1 s spectra (Fig. S8). Minor features were attributed to either surface degradation, residual solvent or adventitious sources. Individual crystalline Cu-SAT particles prepared in flow were further characterized by SED and STEM-EDS. Fig. S9 presents annular dark field STEM and corresponding electron diffraction patterns indexed to our reported Cu-SAT structure. Elemental mapping by STEM-EDS confirmed a homogeneous distribution of constituent elements Cu, S, O, N and C across individual single crystals (Fig. S10).

We next turned to a systematic exploration of the response of the millifluidic synthesis platform for Cu-SAT. Factorial experimental design enabled examination of all possible combinations of reaction parameters. The growth of MOF crystals is usually affected by reaction temperature, time, and concentration of reagents, with reaction yield and sample size being determined by these parameters. In our flow reactor, we can run continuous synthesis with reaction temperatures ranging between 80 and 90 °C, residences time from 60 to 120 min and reagent concentrations between 0.026 and 0.038 mmol mL^{-1}. In order to understand the trade-off between the continuous reaction parameters and the results, a factorial DoE with 8 experiments was created by varying each parameter between the lower and upper bounds and with 3 repeats at intermediate values. The standard deviations for yield, particle size, and particle size IQR in these 3 repeated experiments were 0.58%, 1.5 μm, and 1.4 μm, respectively. Fig. S2 shows a visualization of this design. The designed experiments with the different reaction parameters and the corresponding results for reaction yield, particle size, and particle size IQR are listed in Table 2.

Fig. 5 presents light micrographs of continuously synthesized samples together with box plots of particle size. Keeping the temperature constant at 80 °C but increasing the reaction time from 60 to 120 min resulted in an increased yield from 13 to 50%. Particle sizes likewise increased with reaction time (Fig. 5a and b) with the median particle size increasing from 35 to 81 μm but with an increase in the spread of

Table 1

Comparison of the yield (Y), production rate (PR), and space–time yield (STY) for batch and continuous millifluidic syntheses of Cu-SAT across selected temperature (T), reaction (or residence) time (RT), and concentration of reagents (COR). The standard deviation of the yield in continuous synthesis is 1%, and in batch reaction with or without stirring is 3%. Yields of batch reaction at 80 and 90 °C with 60 min reaction time were too low to provide a precise value.

Parameters			Batch			Batch (stirred)			Continuous		
T (°C)	RT (min)	COR (mmol/mL)	Y (%)	PR (mg/h)	STY (kg/m³/day)	Y (%)	PR (mg/h)	STY (kg/m³/day)	Y (%)	PR (mg/h)	STY (kg/m³/day)
80	60	0.038	–	–	–	64	22	26.5	13	31	41.3
90	60	0.038	–	–	–	67	23	27.7	41.5	99	131.7
80	120	0.038	36	6	7.45	82	14	16.9	49.5	59	78.6
90	120	0.038	62	11	12.8	92	16	19.0	81.5	97	129.3
85	90	0.032	39	9	10.8	67	15	18.5	58	92	122.7
85	90	0.032	41	9	11.3	73	17	20.1	58	92	122.7

Table 2

Reaction parameters of 11 separate experiments used in a factorial design approach and the corresponding reaction results. Abbreviations in this table: Reaction temperature (T), Residence time (RT), Concentration of reagents (COR), Particle size (PS), Particle size interquartile range (PSIQR).

Experiments	T (°C)	RT (min)	COR (mmol/mL)	PS (mmol/mL)	PSIQR (μm)	Yield (%)
1	80	60	0.026	32	23	10.5
2	90	60	0.026	89	48	38.5
3	80	120	0.026	73	32	38
4	90	120	0.026	223	89	78
5	80	60	0.038	35	13	13
6	90	60	0.038	101	51	41.5
7	80	120	0.038	81	21	49.5
8	90	120	0.038	282	120	81.5
9	85	90	0.032	90	48	58
10	85	90	0.032	92	49	58
11	85	90	0.032	93	50	59

particles sizes reflected in an increased particle size IQR from 13 to 21 μm. Reducing the reagent concentrations (from 0.038 to 0.026 mmol/mL) resulted in a reduced yield of 38% (Fig. 5c) with a moderate reduction in median particle size (73 μm) and a substantially broadened

particle size distribution (particle size IQR 32 μm).

Similar trends were observed at 90 °C (Fig. 5e-h) with a doubling of the reaction time giving rise to an increased yield from 42% to 82%. Much larger particles were produced with median particle sizes at 90 °C recorded at 101 and 282 μm (particle size IQR 51 and 120 μm), respectively. As for the lower temperature synthesis, a small reduction in particle size (223 μm) and yield was observed when using a reduced concentration of reagents (Fig. 5g). Notably, a change in the response of the particle size dispersity (particle size IQR) was observed when reducing reagent concentrations at 90 °C. Whereas at lower temperature, the spread of sizes *increased* for reduced concentrations, the particle size IQR instead *decreased* at higher temperature for the more dilute reaction conditions.

Fig. S11 presents SEM micrographs of samples made using the millifluidic reactor across a range of operating parameters. The crystals consistently presented smooth surfaces with sharp faceting. To aid in additional visualization, Figs. S12 and S13 show histograms and box plots of particle size for millifluidic reaction products. Together, the observations on particle size consistently show that larger crystals were produced for longer reaction times and higher reaction temperatures.

Using the results from the 11 experiments of the DoE, linear response surface modelling was used to identify the trade-offs between the reaction parameters and the reaction yield and particle size dispersity. The fitted regression equations for yield, particle size and particle size IQR
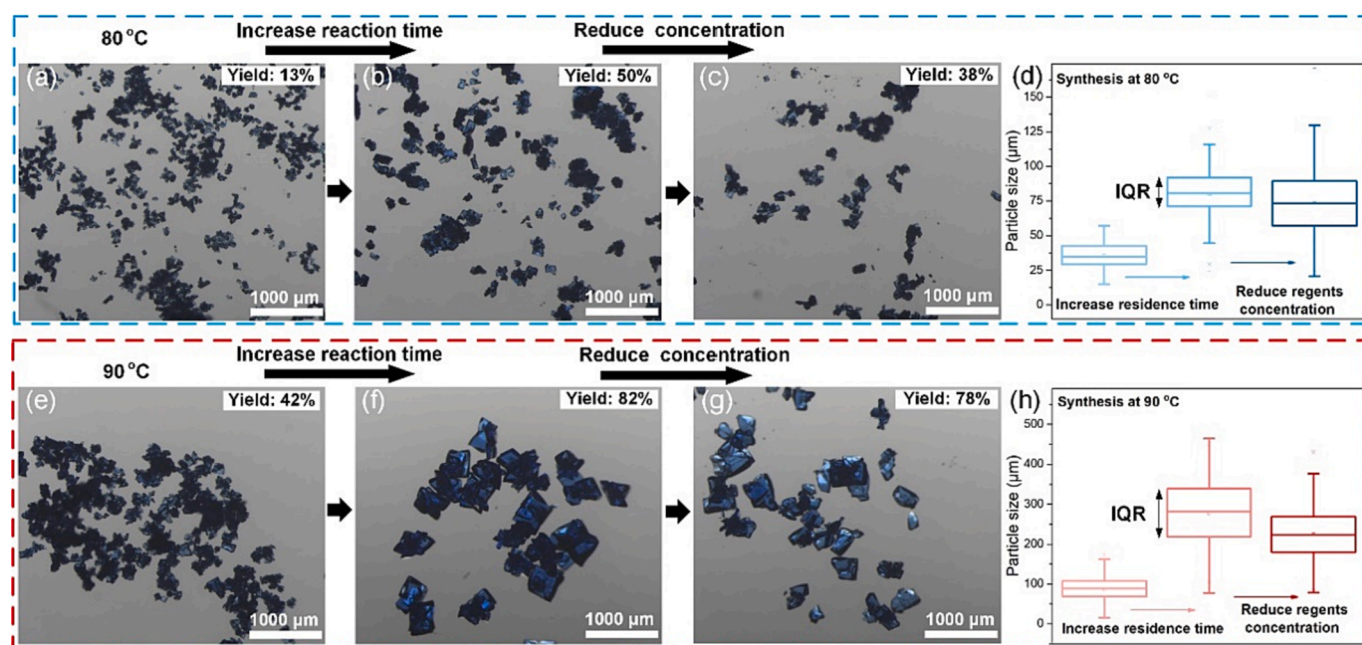

Fig. 5. Cu-SAT particle size results for different continuous reaction conditions. Light micrographs of Cu-SAT made at 80 °C in flow: (a) 60 min residence time, (b) 120 min residence time, (c) 120 min residence time with a lower concentration of reagents, together with (d) a B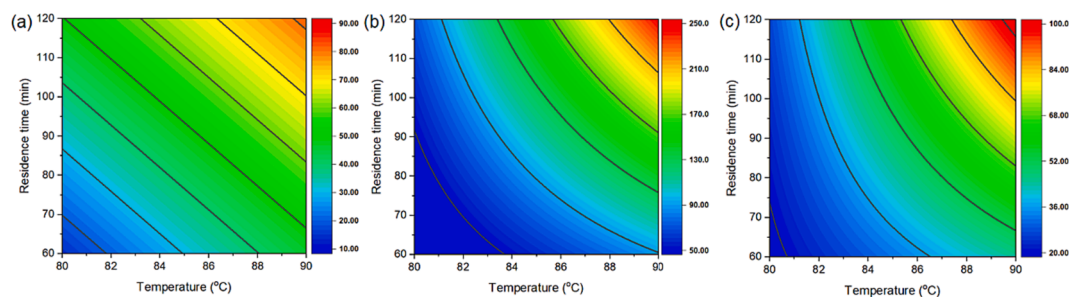ox plot of the particle size in the three samples. Light Micrographs of Cu-SAT made at 90 °C in flow, (e) 60 min residence time, (f) 120 min residence time, (g) 120 min residence time with a lower concentration of reagents, together with (h) a Box plot of the particle size in the three samples.

Fig. 6. Linear response surface modelling results based on DoE. Contour plots of: (a) reaction yield (b) particle size and (c) particle size IQR as a function of synthesis temperature and time with concentration of reagents all equal to 0.032 mmol/ml.

are given in Table S7, here we focus on the key terms and trends. Fig. 6a depicts the contour plot of the fitted response for reaction yield. The response is primarily affected by synthesis temperature and time in linear terms. The response of particle size was similarly found to depend on reaction time and temperature as well as one further statistically significant cross-term between time and temperature (Fig. 6b). A more complex response was determined for particle size IQR (Fig. 6c). The response of particle size IQR included significant contributions from reaction temperature, time, concentration of reagents and their cross terms. In these three equations, a minimal set of terms was used, keeping only terms that showed strong effects in an analysis of variance. The limited number of conditions constrains the model complexity, and there is potential for overfitting for a large number of coefficients as retained for the particle size IQR analysis. Nevertheless, our main finding in particle size IQR is that the response incorporates a more complex dependence.

The linear response modelling approach here is largely phenomenological, requiring wider refinement of MOF crystallization and growth models to gain additional mechanistic insights. However, this approach outlines a route for using a small number of experiments to rapidly identify characteristics of synthetic response. The contour plots exhibit a striking resemblance to a factorial DoE approach applied to the hydrothermal synthesis of MIL-88A(Fe), requiring the use of two-variable terms (cross-terms or quadratic terms) for particle size response characteristics [76]. Wider application to other systems will support the development of a library of similar and distinctive response

characteristics for different MOF chemistries or reactors.

The shape of these response surfaces, nevertheless, do provide a qualitative method to assess prevailing MOF crystal growth theories. The dominant mechanism controlling crystal growth, whether determined by the rate of nucleation events (and whether homogeneous or autocatalytic [76–78]) or the rate of crystal growth, has often been a goal in MOF kinetics studies, whether applying Avrami- or Gualtieri-type kinetic models [79]. Many carboxylate-based MOFs including HKUST-1 [80], MIL-101(Al) [81], and MIL-88A(Fe) [76] show a dominant effect of the faster nucleation rate (i.e. a lower activation energy for nucleation than for growth). Similar characteristics are also seen in polymers, cast instead in terms of initiation and propagation rates [82], integral steps also identified in modelling MOF kinetics [78]. As for polymers, MOFs exhibiting a lower activation energy for nucleation (initiation) will see a broadened particle size (molecular weight) distribution or polydispersity at increased temperature. This is likewise the characteristic behavior observed in millifluidic synthesis of Cu-SAT, with more dilute conditions additionally reducing the driving force for nucleation and thereby reducing the dispersity (particle size IQR). We therefore infer that Cu-SAT exhibits the predominant characteristics of nucleation-dominated crystallization. Further kinetic studies exploring short-timescale crystallization in Cu-SAT may offer additional testing of this hypothesis, but this is beyond the focus of the millifluidic reactor parameter optimization for Cu-SAT production.

Instead, we apply the linear response modelling to a Pareto front determination. Controlled MOF crystal growth offers a route to the maximization of yield, but simultaneously supports minimization of particle size dispersity, outlining a multi-objective challenge. Fig. 7 presents a plot highlighting the results in terms of these two objective axes, yield and particle size IQR. Light grey points are generated from the simulated equations for yield and particle size IQR, showing the linear response model values, and blue points mark the experimental data points. This plot further validates the model fit, with the distribution of the experimental data points captured by the shape of the predictions made by the response surface. Deviations between the experiment and model values reflects the precision offered in the analysis. The root mean square error (RMSE) of yield and particle size IQR comparing model and experimental DoE values were 4.9% and 2.5 μm, respectively. The Pareto front was, in turn, extracted from discrete evaluation of the linear response surface model, with the maximum yield and minimum particle size IQR highlighted in red. These points establish the set of optima possible within the constraints of the reactor operating parameters, highlighting the trade-off between increasing yield and sacrificing a narrow particle size distribution. Alternative reactor designs supporting smaller slug sizes while retaining a stable slug flow pattern may present routes to modifying this trade-off.

To further establish the predictive value of the linear response model within the existing operating parameters, we selected a model value (Fig. 7) on the Pareto front for reaction conditions of 90 min residence time at 80 °C with reagent concentration of 0.038 mmol mL^{-1}. The experimental reaction at these conditions exhibited matched yield and
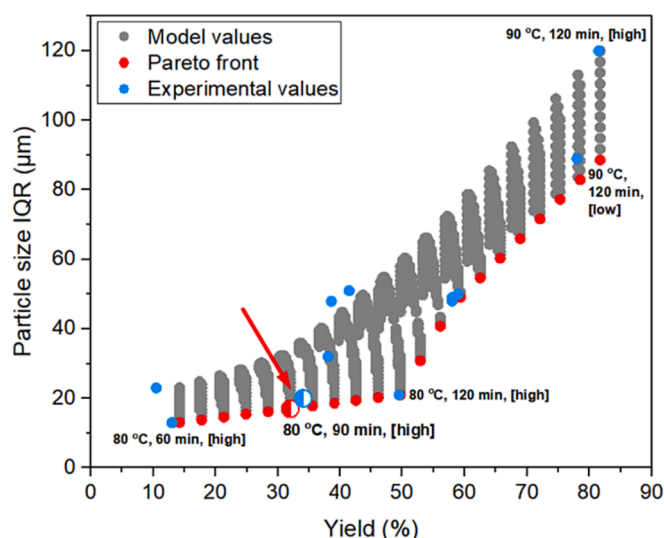

Fig. 7. Pareto front plot of yield to particle size IQR. Experimental values are shown in blue. Model values are shown in gray with the Pareto front marked in red. Half-filled circles show selected conditions for comparing the model (red) and experimental response (blue). (For interpretation of the references to color in this figure legend, the reader is referred to the web version of this article.)
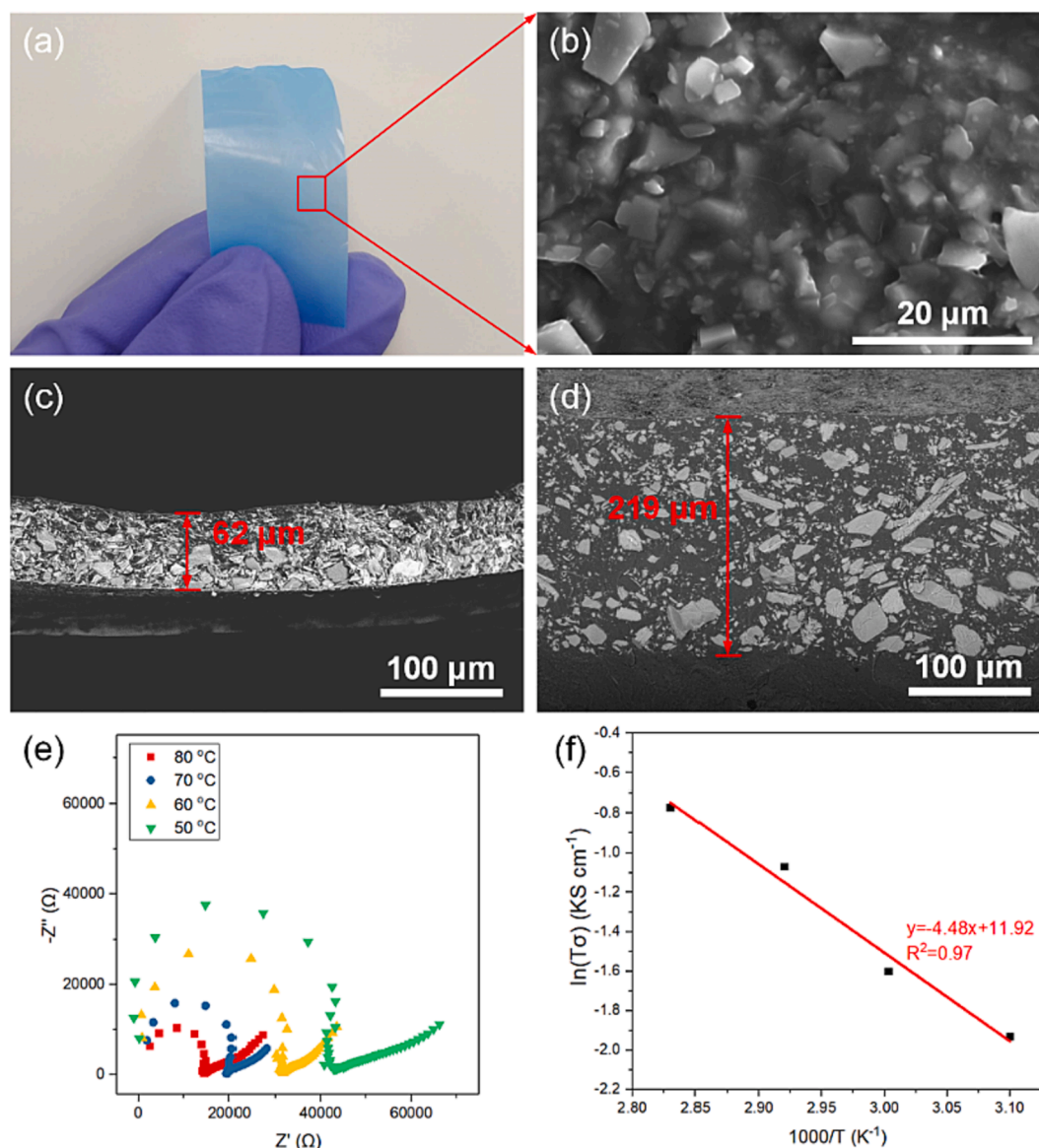
Fig. 8. Results of proton conduction membrane fabrication using continuously synthesized Cu-SAT: (a) Digital and (b) SEM images of MMM-60 wt%, and cryo SEM micrographs of cross section of (c) the dry membrane and (d) the fully hydrated MMM-60 wt%, (e) Nyquist plots depicting the complex impedance as measured by electrochemical impedance spectroscopy and (f) Arrhenius plots of MMM-60 wt% conductivities for different temperatures at 95 % RH.

particle size IQR. The experimental yield differed from the model by 2% (34% for experimental yield compared to a 32% predicted yield), a small difference in the context of yields spanning approximately 15 to 85%. The experimental particle size IQR differed from the model by 3 μm (20 μm for experimental particle size IQR as compared with a 17 μm predicted IQR), likewise small relative to the range of particle size IQR values recorded from approximately 10 to 120 μm. The results of this validation experiment were also consistent with the variation expected from the RMSE for yield and particle size IQR (4.9% and 2.5 μm, respectively). This minimal, systematic DoE approach with robust interpolation across significant variation in yield and particle size distribution characteristics provides a step toward benchmarking and comparison of the multi-parameter response of MOF growth between other sulfonate and non-sulfonate MOFs.

3.3. Membrane fabrication and proton conductivity measurements

MMMs were fabricated using Cu-SAT prepared by millifluidic synthesis in order to demonstrate the proton-conducting properties and

potential use in fuel cell applications. MMMs were prepared using 60 wt % Cu-SAT and a blend of PVP and PVDF, matching previous MMM designs for Cu-SAT [15]. Fig. 8a shows a digital photograph of MMM-60 wt %, exhibiting a similar blue color to Cu-SAT. The Cu-SAT particles were incorporated throughout the polymer matrix (Fig. 8b). Cryo-SEM was used to determine the hydrated membrane thickness, as the polymer membrane swells during water uptake. As shown in Fig. 8c and d, the thickness of dry membrane was approximately 62 μm and increased to approximately 219 μm when fully hydrated, attributed to the hydrophilic behavior of PVP. Figs. S14 and S15 in the SI show EDS mapping of the membrane both in plan view and in cross section, further confirming the dispersion of the MOF particles throughout the membrane. Fig. S16 shows X-ray computed tomography of MMM-60 wt%, presented in orthogonal slices through the tomographic volume as well as in a volume rendering. 3D analysis indicated some asymmetry in the distribution of the largest particles but corroborates the distribution of Cu-SAT throughout the composite membrane. Further refinements of particle size control and membrane casting may enhance overall membrane performance further.

Fig. 8e shows the EIS results of MMM-60 wt% tested under different temperatures at 95% RH. The resistance decreased from $4.29 \times 10^3 \, \Omega$ to $1.45 \times 10^3 \, \Omega$ as the temperature increased from 50 to 80 °C, enabling determination of the activation energy E_a (Fig. 8f). The activation energy of MMM-60 wt% was determined to be 37 ± 3 kJ mol^{-1} or 0.39 ± 0.04 eV (uncertainties given as the standard error), a value consistent with a predominantly Grotthuss mechanism, which ranges from 14 to 40 kJ mol^{-1} ($E_a < 0.4$ eV) [83]. The proton conductivity results of MMM-60 wt% determined using CV showed results similar to those by EIS, the highest proton conductivity recorded by CV as 1.26 mS cm^{-1} at 80 °C in 95% RH, and the E_a determined from CV (Fig. S17c and d) was 35 ± 4 kJ mol^{-1} or 0.36 ± 0.04 eV (uncertainties given as the standard error).

The best proton conductivity of MMM-60 wt% determined by EIS was 1.34 ± 0.05 mS cm^{-1} at 80 °C and 95% RH, surpassing previous reports for Cu-SAT PVP/PVDF membranes of 0.8 mS cm^{-1} at 80 °C and 98% RH [15]. A full set of proton conductivities for MMM-60 wt% determined by EIS and CV in 95% RH and at different temperatures is given in Table S8 and S9. The MMM-60 wt% membrane reported here compares favorably to recently reported MOFs or MOF-based PEMs, such as phosphonate-based MOFs with a proton conductivity of 0.05 mS cm^{-1} at 90 °C and 98% RH [84], phenyl acyl thiourea carboxylate-based MOFs with a proton conductivity of 0.18 mS cm^{-1} at 100 °C and 98% RH [68], Ni-MOFs in a polyacrylonitrile nanofiber membrane with a proton conductivity of 0.06 mS cm^{-1} at 90 °C and 90% RH [85], and Cu-MOF/ PVP/PVDF composite membrane with a proton conductivity up to 0.44 mS cm^{-1} at 80 °C and 98% RH [86]. While these comparisons are not exhaustive and encompass many complex variables, millifluidic-synthesized Cu-SAT represents a competitive candidate material for further development of MMMs for fuel cell applications. Extending the stability of Cu-SAT and optimization of the interplay of mechanical and chemical properties of the Cu-SAT-polymer membrane offer routes to further improvements in composite performance. MOFs developed for these applications tend to be tested as pellets or as MMMs without reported particle size optimization [11,15,87,88], and work on controlled particle size is underway to pursue this route to further advances in MMM design.

4. Conclusions

We have synthesized Cu-SAT, a mixed linker MOF incorporating both sulfonate and amine groups and carried out single crystal structure determination, significant materials characterization, and evaluation of synthetic parameters. Cu-SAT synthesis was transferred from batch solvothermal synthesis to a continuous synthesis using a millifluidic flow reactor, demonstrating more than five hours sustained production rate and consistent sample quality. The reactor parameters enable facile control of Cu-SAT particle size and particle size dispersity by adjusting residence time, temperature, and reagent concentration. We have employed a factorial DoE approach to quantify these trends, extracting a predictive linear response model indicating nucleation driven-growth processes. The reaction yields in the flow reactor were 10 to 20 % higher than corresponding batch reactions using the same reaction parameters, indicating improved mass and heat transfer in flow synthesis. These findings establish a new mode of sulfonate MOF synthesis in a generalizable, fouling-free slug-flow reactor.

Finally, the continuously synthesized Cu-SAT MOF was incorporated with PVP and PVDF polymers for PEMs application, and this membrane presented a proton conductivity of 1.34 ± 0.05 mS cm^{-1} at 80 °C and 95% RH. Further engineering of the membrane internal interfaces, mixed membrane composition, and optimization of particle size for MMMs, offer routes to the implementation of composite MOF materials for fuel cell applications, underpinned by reproducible sulfonate MOF crystal growth in continuous flow synthesis.

Declaration of Competing Interest

The authors declare no competing interests.

Data availability

Data will be made available on request.

Appendix A. Supplementary data

CCDC 2247539 contains the supplementary crystallographic data for this paper. These data can be obtained free of charge from The Cambridge Crystallographic Data Centre via www.ccdc.cam.ac.uk/data_request/cif. Supplementary data to this article can be found online at https://doi.org/10.1016/j.cej.2023.145892.

References

[1] T. Ghanbari, F. Abnisa, M. Wan, A Review on Production of Metal Organic Frameworks (MOF) for CO2 Adsorption, Sci. Total Environ. 707 (2019), 135090.

[2] K. Wang, Y. Li, L.-H. Xie, X. Li, J.-R. Li, Construction and application of base-stable MOFs: a critical review, Chem. Soc. Rev. 51 (15) (2022) 6417–6441.

[3] X.L. Hu, K. Wang, X. Li, Q.Q. Pan, Z.M. Su, Two Anthracene Chromophores based Metal-Organic Frameworks for Gas Absorption and Promising Nitro Aromatic Sensing, New J. Chem. 44 (2020) 1249–1252.

[4] H. Li, K. Wang, Y. Sun, C.T. Lollar, J. Li, H.-C. Zhou, Recent advances in gas storage and separation using metal–organic frameworks, Mater. Today 21 (2) (2018) 108–121.

[5] D. Lv, P. Zhou, J. Xu, S. Tu, F. Xu, J. Yan, H. Xi, W. Yuan, Q. Fu, X. Chen, Q. Xia, Recent advances in adsorptive separation of ethane and ethylene by C$_2$H$_6$-selective MOFs and other adsorbents, Chem. Eng. J. 431 (2022) 133208–133230.

[6] L. Mitchell, B. Gonzalez-Santiago, J.P.S. Mowat, M.E. Gunn, P. Williamson, N. Acerbi, M.L. Clarke, P.A. Wright, CCYG, Remarkable Lewis acid catalytic performance of the scandium trimesate metal organic framework MIL-100(Sc) for C-C and C-N bond-forming reactions, Catal. Sci. Technol. 3 (3) (2013) 606–617.

[7] D. Yang, B.C. Gates, Catalysis by Metal Organic Frameworks: Perspective and Suggestions for Future Research, ACS Catal. 9 (2019) 1779–1798.

[8] D.-W. Lim, H. Kitagawa, Proton Transport in Metal-Organic Frameworks, Chem. Rev. 120 (16) (2020) 8416–8467.

[9] D.-W. Lim, H. Kitagawa, Rational strategies for proton-conductive metal-organic frameworks, Chem. Soc. Rev. 50 (11) (2021) 6349–6368.

[10] G.-M. Wu, M.-Y. Zhang, F.-D. Wang, C.-X. Zhang, Q.-L. Wang, A dual-function Cd-MOF with high proton conduction and excellent fluorescence detection of pyridine, Dalton T. 51 (17) (2022) 6687–6695.

[11] Y. Li, J. Feng, L. Wang, G. Li, High proton conduction in two highly stable phenyl imidazole dicarboxylate-based Cd(II)-MOFs, J. Solid State Chem. 319 (2023), 123828.

[12] K. Biradha, A. Goswami, R. Moi, S. Saha, Metal–organic frameworks as proton conductors: strategies for improved proton conductivity, Dalton T. 50 (2021) 10655–10673.

[13] H.A. Patel, N. Mansor, S. Gadipelli, D.J.L. Brett, Z. Guo, Superacidity in Nafion/ MOF Hybrid Membranes Retains Water at Low Humidity to Enhance Proton Conduction for Fuel Cells, ACS Appl. Mater. Inter. 8 (45) (2016) 30687–30691.

[14] G. Zhang, H. Fei, Synthesis and Applications of Porous Organosulfonate-Based Metal-Organic Frameworks, Top. Curr. Chem. 377 (2019) 32.

[15] R. Moi, A. Ghorai, S. Banerjee, K. Biradha, Amino and Sulfonate Functionalized Metal-Organic Framework for Fabrication of Proton Exchange Membranes with Improved Proton Conductivity, Cryst. Growth Des. 20 (8) (2020) 5557–5563.

[16] A.V. Desai, B. Joarder, A. Roy, P. Samanta, R. Babarao, S.K. Ghosh, Multifunctional Behavior of Sulfonate-Based Hydrolytically Stable Microporous Metal-Organic Frameworks, ACS Appl. Mater. Inter. 10 (45) (2018) 39049–39055.

[17] Z. Li, G. He, Y. Zhao, Y. Cao, H. Wu, Y. Li, Z. Jiang, Enhanced proton conductivity of proton exchange membranes by incorporating sulfonated metal-organic frameworks, J. Power Sources 262 (2014) 372–379.

[18] X.Y. Dong, J.H. Wang, S.S. Liu, Z. Han, Q.J. Tang, Synergy between isomorphous acid and basic MOFs for anhydrous proton conduction of low-cost hybrid membranes at high temperature, ACS Appl, Mater. Inter. 10 (2018) 38209–38216.

[19] V.V. Butova, A.P. Budnyk, E.A. Bulanova, C. Lamberti, A.V. Soldatov, Hydrothermal synthesis of high surface area ZIF-8 with minimal use of TEA, Solid State Sci. 69 (2017) 13–21.

[20] S.N. Tambat, P.K. Sane, S. Suresh, N. Varadan, O.A.B. Pandit, S.M. Sontakke, Hydrothermal synthesis of NH$_2$-UiO-66 and its application for adsorptive removal of dye, Adv. Powder Technol. 29 (11) (2018) 2626–2632.

[21] C.-G. Lin, W. Zhou, X.-T. Xiong, W. Xuan, P.J. Kitson, D.-L. Long, W. Chen, Y.-F. Song, L. Cronin, Digital Control of Multistep Hydrothermal Synthesis by Using 3D Printed Reactionware for the Synthesis of Metal-Organic Frameworks, Angew. Chem. Int. Ed. 57 (51) (2018) 16716–16720.

[22] B. Zhang, Y. Luo, K. Kanyuck, N. Saenz, K. Reed, P. Zavalij, J. Mowery, G. Bauchan, Facile and template-free solvothermal synthesis of mesoporous/macroporous metal–organic framework nanosheets, RSC Adv. 8 (58) (2018) 33059–33064.

[23] L.A. Lozano, C.M. Iglesias, B.M.C. Faroldi, M.A. Ulla, J.M. Zamaro, Efficient solvothermal synthesis of highly porous UiO-66 nanocrystals in dimethylformamide-free media, J. Mater. Sci. 53 (3) (2018) 1862–1873.

[24] K. Kamal, M.A. Bustam, M. Ismail, D. Grekov, A. Mohd Shariff, P. Pre, Optimization of Washing Processes in Solvothermal Synthesis of Nickel-Based MOF-74, Materials 13 (2020) 2741.

[25] A.R. Abbasi, M. Rizvandi, Influence of the ultrasound-assisted synthesis of Cu-BTC metal-organic frameworks nanoparticles on uptake and release properties of rifampicin, Ultrason. Sonochem. 40 (2018) 465–471.

[26] A. Bakhshi, H. Saravani, G. Sargazi, M. Shahbakhsh, Ultrasound-assisted efficient synthesis of a novel Nd–MOF polymer as a new candidate for electrocatalytic activity in hydrogen storage, J. Appl. Electrochem. 51 (3) (2021) 399–410.

[27] C. Forsyth, T. Taras, A. Johnson, J. Zagari, C. Collado, M.M. Hoffmann, C.R. Reed, Microwave Assisted Surfactant-Thermal Synthesis of Metal-Organic Framework Materials, Appl. Sci. 10 (2020) 4563.

[28] A. Laybourn, J. Katrib, R.S. Ferrari-John, C.G. Morris, S. Yang, O. Udoudo, T. L. Easun, C. Dodds, N.R. Champness, S.W. Kingman, M. Schröder, Metal–organic frameworks in seconds via selective microwave heating, J. Mater. Chem. A 5 (16) (2017) 7333–7338.

[29] I. Thomas Hillman, L.A. Stevens, M. Lange, J. Mllmer, W. Lewis, C. Dodds, S. W. Kingman, A. Laybourn, Developing a sustainable route to environmentally relevant metal–organic frameworks: ultra-rapid synthesis of MFM-300(Al) using microwave heating, Green Chem. 21 (2019) 5039–5045.

[30] D. Rambabu, S. Bhattacharyya, T. Singh, L.C.M.T.K. Maji, Stabilization of MAPbBr 3 Perovskite Quantum Dots on Perovskite MOFs by a One-Step Mechanochemical Synthesis, Inorg. Chem. 59 (2) (2020) 1436–1443.

[31] J. Yang, X. Feng, G. Lu, Y. Li, C. Mao, Z. Wen, W. Yuan, NaCl as a solid solvent to assist the mechanochemical synthesis and post-synthesis of hierarchical porous MOFs with high I$_2$ vapour uptake, Dalton T. 47 (14) (2018) 5065–5071.

[32] V.M.V.G. Nageswaran, Review—Direct Electrochemical Synthesis of Metal Organic Frameworks, J. Electrochem. Soc. 167 (2020), 155527.

[33] L.-L. Jiang, X. Zeng, M. Li, M.-Q. Wang, T.-Y. Su, X.-C. Tian, J. Tang, Rapid electrochemical synthesis of HKUST-1 on indium tin oxide, RSC Adv. 7 (15) (2017) 9316–9320.

[34] A. Manz, J.C. Fettinger, E. Verpoorte, H. Lüdi, H.M. Widmer, D.J. Harrison, Micromachining of monocrystalline silicon and glass for chemical analysis systems A look into next century's technology or just a fashionable craze?, Trac-Trend, Anal. Chem. 10 (5) (1991) 144–149.

[35] J. Wang, Y. Song, Microfluidic Synthesis of Nanohybrids, Small 13 (2017) 1604084.

[36] I. Rossetti, M. Compagnoni, Chemical reaction engineering, process design and scale-up issues at the frontier of synthesis: Flow chemistry, Chem. Eng. J. 296 (2016) 56–70.

[37] O. Długosz, M. Banach, Inorganic nanoparticle synthesis in flow reactors – applications and future directions, React, Chem. Eng. 5 (9) (2020) 1619–1641.

[38] C.T. Kung, H.Y. Gao, C.Y. Lee, Y.N. Wang, W.J. Dong, C.H. Ko, G. Wang, L.M. Fu, Microfluidic synthesis control technology and its application in drug delivery, bioimaging, biosensing, environmental analysis and cell analysis, Chem. Eng. J. 399 (2020), 125748.

[39] X. Wang, J. Liu, P. Wang, D. Andrew, L. Feng, X. Zhu, W. Wen, K. Rimantas, X. Gong, Synthesis of Biomaterials Utilizing Microfluidic Technology, Genes 9 (2018) 283.

[40] L. Falk, J.-M. Commenge, Performance comparison of micromixers, Chem. Eng. Sci. 65 (1) (2010) 405–411.

[41] R. Munirathinam, J. Huskens, W. Verboom, Supported Catalysis in Continuous-Flow Microreactors, Adv. Synth. Catal. 357 (6) (2015) 1093–1123.

[42] C. Echaide-Górriz, C. Clément, F. Cacho-Bailo, C. Téllez, J. Coronas, New strategies based on microfluidics for the synthesis of metal–organic frameworks and their membranes, J. Mater. Chem. A 6 (14) (2018) 5485–5506.

[43] J. Ren, X. Dyosiba, N.M. Musyoka, H.W. Langmi, M. Mathe, S. Liao, Review on the current practices and efforts towards pilot-scale production of metal-organic frameworks (MOFs), Coordin, Chem. Rev. 352 (2017) 187–219.

[44] P. Coliaie, R.R. Bhawnani, A. Prajapati, R. Ali, P. Verma, G. Giri, M.S. Kelkar, A. Korde, M. Langston, C. Liu, N. Nazemifard, D. Patience, T. Rosenbaum, D. Skliar, N.K. Nere, M.R. Singh, Patterned microfluidic devices for rapid screening of metal-organic frameworks yield insights into polymorphism and non-monotonic growth, Lab Chip 22 (2) (2022) 211–224.

[45] M. Faustini, J. Kim, G.-Y. Jeong, J.Y. Kim, H.R. Moon, W.-S. Ahn, D.-P. Kim, Microfluidic approach toward continuous and ultrafast synthesis of metal-organic framework crystals and hetero structures in confined microdroplets, J. Am. Chem. Soc. 135 (39) (2013) 14619–14626.

[46] H. Lu, H. Wang, Y. Liu, M. Wang, J. Hu, Q. Yang, Substance transfer behavior controlled by droplet internal circulation, Chem. Eng. J. 393 (2020), 124657.

[47] A.M. Nightingale, T.W. Phillips, J.H. Bannock, J.C. de Mello, Controlled multistep synthesis in a three-phase droplet reactor, Nat. Commun. 5 (2014) 3777.

[48] T. Bailey, M. Pinto, N. Hondow, K.J. Wu, Continuous microfluidic synthesis of zirconium-based UiO-67 using a coiled flow invertor reactor, MethodsX 8 (2021), 101246.

[49] H.-Y. Wu, C.-L. Wu, W. Liao, B.M. Matsagar, K.-Y. Chang, J.-H. Huang, K.-W. Wu, Continuous and ultrafast MOF synthesis using droplet microfluidic nanoarchitectonics, J. Mater. Chem. A 11 (17) (2023) 9427–9435.

[50] N. Rohra, G. Gaikwad, P. Dandekar, R. Jain, Microfluidic Synthesis of a Bioactive Metal-Organic Framework for Glucose-Responsive Insulin Delivery, ACS Appl. Mater. Inter. 14 (6) (2022) 8251–8265.

[51] Q. Fu, W. Niu, L. Yan, W. Xie, H. Jiang, S. Zhang, L. Yang, Y. Wang, Y. Xing, X. Zhao, A versatile microfluidic strategy using air–liquid segmented flow for continuous and efficient synthesis of metal–organic frameworks, Mater. Lett. 343 (2023), 134344.

[52] S. Kevat, B. Sutariya, V.N. Lad, Microfluidics-assisted, time-effective and continuous synthesis of bimetallic ZIF-8/67 under different synthesis conditions, J. Mater. Sci. 58 (12) (2023) 5219–5233.

[53] S. Yamada, A. Hirano, Y. Tanaka, R. Akiyoshi, H. Yoshikawa, D. Tanaka, Synthesis of Mixed-Metal MIL-68 under Mild Conditions by Controlling Nucleation Using a Microfluidic System, Cryst. Growth Des. 22 (7) (2022) 4139–4145.

[54] G. Xu, K. Otsubo, T. Yamada, S. Sakaida, H. Kitagawa, Superprotonic conductivity in a highly oriented crystalline metal–organic framework nanofilm, J. Am. Chem. Soc. 135 (2013) 7438.

[55] X.-Y. Dong, J.-J. Li, Z. Han, P.-G. Duan, L.-K. Li, S.-Q. Zang, Tuning the functional substituent group and guest of metal–organic frameworks in hybrid membranes for improved interface compatibility and proton conduction, J. Mater. Chem. A 5 (7) (2017) 3464–3474.

[56] S.M. Rezaei Niya, M. Hoorfar, Study of proton exchange membrane fuel cells using electrochemical impedance spectroscopy technique – A review, J. Power Sources 240 (2013) 281–293.

[57] N.A. Nazir, N. Kim, W.G. Iglesias, A. Jakli, T. Kyu, Conductive behavior in relation to domain morphology and phase diagram of Nafion/poly(vinylidene-co-trifluoroethylene) blends, Polymer 53 (1) (2012) 196–204.

[58] M.A. Hickner, H. Ghassemi, Y.S. Kim, B.R. Einsla, J.E. McGrath, Alternative Polymer Systems for Proton Exchange Membranes (PEMs), Chem. Rev. 104 (10) (2004) 4587–4612.

[59] J. Dechnik, J. Gascon, C.J. Doonan, C. Janiak, C.J. Sumby, Mixed-Matrix Membranes, Angew. Chem. Int. Ed. 56 (32) (2017) 9292–9310.

[60] F.u. Liu, N.A. Hashim, Y. Liu, M.R.M. Abed, K. Li, Progress in the production and modification of PVDF membranes, J. Membrane. Sci. 375 (1-2) (2011) 1–27.

[61] Y. Zhang, J. Li, L. Ma, W. Cai, H. Cheng, Recent Developments on Alternative Proton Exchange Membranes: Strategies for Systematic Performance Improvement, Energy Technol. 3 (2015) 675–691.

[62] C. Wu, S. Lu, H. Wang, X. Xu, S. Peng, Q. Tan, Y. Xiang, A novel polysulfone–polyvinylpyrrolidone membrane with superior proton-to-vanadium ion selectivity for vanadium redox flow batteries, J. Mater. Chem. A 4 (4) (2016) 1174–1179.

[63] G.M. Sheldrick, SHELXT - integrated space-group and crystal-structure determination, Acta Crystallographica Section A 71 (2015) 3–8.

[64] G.M. Sheldrick, Crystal structure refinement with SHELXL, Acta Crystallogr. C 71 (2015) 3–8.

[65] S. Li, S. Yu, S.M. Collins, D.N. Johnstone, C.W. Ashling, A.F. Sapnik, P.A. Chater, D. S. Keeble, L.N. McHugh, P.A. Midgley, D.A. Keen, T.D. Bennett, A new route to porous metal–organic framework crystal–glass composites, Chem. Sci. 11 (36) (2020) 9910–9918.

[66] B.W. Veal, P.M. Baldo, A.P. Paulikas, J.A. Eastman, Understanding Artifacts in Impedance Spectroscopy, J. Electrochem. Soc. 162 (1) (2015) H47–H57.

[67] L.i. Ding, H. Zou, J. Lu, H. Liu, S. Wang, H. Yan, Y. Li, Enhancing Proton Conductivity of Nafion Membrane by Incorporating Porous Tb-Metal-Organic Framework Modified with Nitro Groups, Inorg. Chem. 61 (40) (2022) 16185–16196.

[68] L.X. Xie, Z.J. Ye, X.D. Zhang, G. Li, Two stable phenyl acyl thiourea carboxylate-based MOFs: Syntheses, crystal structures and proton conductive properties, J. Solid State Chem. 311 (2022), 123154.

[69] M. Mamlouk, P. Ocon, K. Scott, Preparation and characterization of polybenzimidzaole/diethylamine hydrogen sulphate for medium temperature proton exchange membrane fuel cells, J. Power Sources 245 (2014) 915–926.

[70] A. Laybourn, A.M. López-Fernández, I. Thomas-Hillman, J. Katrib, W. Lewis, C. Dodds, A.P. Harvey, S.W. Kingman, Combining continuous flow oscillatory baffled reactors and microwave heating: Process intensification and accelerated synthesis of metal-organic frameworks, Chem. Eng. J. 356 (2019) 170–177.

[71] L. Zhong, S.F. Parker, Structure and vibrational spectroscopy of methanesulfonic acid, R. Soc. Open Sci. 5 (2018), 181363.

[72] Y. Ji, X. Yang, Z. Ji, L. Zhu, N. Ma, D. Chen, X. Jia, J. Tang, Y. Cao, DFT-Calculated IR Spectrum Amide I, II, and III Band Contributions of N-Methylacetamide Fine Components, ACS, Omega 5 (15) (2020) 8572–8578.

[73] N. Majoul, S. Aouida, B. Bessaïs, Progress of porous silicon APTES-functionalization by FTIR investigations, Appl. Surf. Sci. 331 (2015) 388–391.

[74] M. Staufer, U. Birkenheuer, T. Belling, F. Nörtemann, N. Rösch, W. Widdra, K.L. Kostov, T. Moritz, D. Menzel, The vibrational structure of benzene adsorbed on Si (001), J. Chem. Phys. 112 (2000) 2498-2506.

[75] Y. Ishida, T. Togashi, K. Yamamoto, M. Tanaka, T. Kiss, T. Otsu, Y. Kobayashi, S. Shin, Time-resolved photoemission apparatus achieving sub-20-meV energy resolution and high stability, Rev. Sci. Instrum. 85 (2014), 123904.

[76] E. Bagherzadeh, S.M. Zebarjad, H.R. Madaah Hosseini, P. Chagnon, Preparation, optimization and evolution of the kinetic mechanism of an Fe-MIL-88A metal–organic framework, CrstEngComm 21 (3) (2019) 544–553.

[77] A.F. Gualtieri, Synthesis of sodium zeolites from a natural halloysite, Phys. Chem. Miner. 28 (10) (2001) 719–728.

[78] A.V. Dighe, L. Huelsenbeck, R.R. Bhawnani, P. Verma, K.H. Stone, M.R. Singh, G. Giri, Autocatalysis and Oriented Attachment Direct the Synthesis of a Metal-Organic Framework, JACS Au 2 (2) (2022) 453–462.

[79] N. Stock, S. Biswas, Synthesis of metal-organic frameworks (MOFs): routes to various MOF topologies, morphologies, and composites, Chem. Rev. 112 (2012) 933–969.

[80] E. Biemmi, S. Christian, N. Stock, T. Bein, High-throughput screening of synthesis parameters in the formation of the metal-organic frameworks MOF-5 and HKUST-1, Micropor. Mesopor. Mat. 117 (1-2) (2009) 111–117.

[81] E. Stavitski, M. Goesten, J. Juan Alcaniz, A. Martinez-Joaristi, P. Serra Crespo, A.V. Petukhov, J. Gascon, F. Kapteijn, Kinetic control of metal-organic framework crystallization investigated by time-resolved in situ X-ray scattering, Angew. Chem. Int. Ed. 50 (2011) 9624–9628.

[82] N.A. Lynd, M.A. Hillmyer, Effects of Polydispersity on the Order−Disorder Transition in Block Copolymer Melts, Macromolecules 40 (22) (2007) 8050–8055.

[83] J.-W. Wang, S.-C. Hsu, Enhanced high-temperature polymer electrolyte membrane for fuel cells based on polybenzimidazole and ionic liquids, Electrochim. Acta 56 (7) (2011) 2842–2846.

[84] M. Rautenberg, B. Bhattacharya, C. Das, F. Emmerling, Mechanochemical Synthesis of Phosphonate-Based Proton Conducting Metal-Organic Frameworks, Inorg. Chem. 61 (28) (2022) 10801–10809.

[85] Z.X. Bai, S.C. Liu, P. Chen, G.J. Cheng, G.Y. Wu, Y. Liu, Enhanced proton conduction of imidazole localized in one-dimensional Ni-metal-organic framework nanofibers, Nanotechnology 31 (2020), 125702.

[86] Y.L. Bao, J.Y. Zheng, H.P. Zheng, G.D. Qi, J.R. An, Y.P. Wu, Y.L. Liu, W.W. Dong, J. Zhao, D.S. Li, Cu-MOF@PVP/PVDF hybrid composites as tunable proton-conducting materials, J. Solid State Chem. 310 (2022), 123070.

[87] Z.-Q. Shi, N.-N. Ji, M.-H. Wang, G. Li, A Comparative Study of Proton Conduction Between a 2D Zinc(II) MOF and Its Corresponding Organic Ligand, Inorg. Chem. 59 (7) (2020) 4781–4789.

[88] X. Wang, Y. Rong, F. Wang, C. Zhang, Q. Wang, High performance proton exchange membranes with double proton conduction pathways by introducing MOF impregnated with protic ionic liquid into SPEEK, Micro. and Meso. Mater. 346 (2022), 112314.